The Astrophysical Journal, 934:165 (7pp), 2022 August 1 https://doi.org/10.3847/1538-4357/ac7f42

Monte Carlo Simulations of Electron Acceleration at Bow Waves Driven by Fast Jets in the Earth's Magnetosheath

Laura Vuorinen[1], Rami Vainio[1], Heli Hietala[1,2], and Terry Z. Liu[3]
[1] Department of Physics and Astronomy, University of Turku, Turku, Finland; laura.k.vuorinen@utu.fi
[2] The Blackett Laboratory, Imperial College London, London, UK
[3] Department of Earth, Planetary, and Space Sciences, University of California, Los Angeles, Los Angeles, CA, USA
Received 2022 January 24; revised 2022 June 21; accepted 2022 July 3; published 2022 August 4

Abstract

The shocked solar wind flows around the Earth's magnetosphere in the magnetosheath downstream of the Earth's bow shock. Within this region, faster flows of plasma, called magnetosheath jets, are frequently observed. These jets have been shown to sometimes exhibit supermagnetosonic speeds relative to the magnetosheath flow and to develop bow waves or shocks of their own. Such jet-driven bow waves have been observed to accelerate ions and electrons. We model electron acceleration by magnetosheath jet-driven bow waves using test-particle Monte Carlo simulations. Our simulations suggest that the energy increase of electrons with energies of a few hundred eV to 10 keV can be explained by a collapsing magnetic trap forming between the bow wave and the magnetopause with shock drift acceleration at the moving bow wave. Our simulations allow us to estimate the efficiency of acceleration as a function of different jet and magnetosheath parameters. Electron acceleration by jet-driven bow waves can increase the total acceleration in the parent shock environment, most likely also at shocks other than the Earth's bow shock.

Unified Astronomy Thesaurus concepts: Planetary bow shocks (1246); Planetary magnetospheres (997); Solar-terrestrial interactions (1473)

1. Introduction

The solar wind flows supermagnetosonically from the Sun, and the Earth's magnetic field acts as an obstacle in this flow. A bow shock forms ahead of the Earth, where the solar wind is slowed to submagnetosonic speeds and can then flow around the magnetosphere in the region called the magnetosheath. Magnetosheath jets are high dynamic pressure flows formed at the Earth's bow shock (see Plaschke et al. 2018, and the references therein). They propagate toward the magnetopause and some of them collide into it, leading to perturbations in the magnetosphere and in the ionosphere. Jets are mostly observed downstream of the quasi-parallel shock (e.g., Plaschke et al. 2013; Archer & Horbury 2013; Vuorinen et al. 2019). One suggested formation mechanism is related to the corrugated nature of the quasi-parallel shock. Hietala et al. (2009) showed with a theoretical treatment of magnetohydrodynamic (MHD) Rankine–Hugoniot jump conditions that solar wind flow through a ripple in the shock can lead to a such a jet. These jets are not rare. Under favorable conditions, i.e., downstream of the quasi-parallel shock and during high solar wind speed intervals, a spacecraft observes several jets per hour in the subsolar magnetosheath (e.g., LaMoury et al. 2021).

Some jets are fast enough to drive their own bow waves or shocks and they have been shown to accelerate ions and electrons in recent observational studies (Liu et al. 2019, 2020a, 2020b). Liu et al. (2020b) presented three case studies of electron acceleration at jet-driven bow waves using Time History of Events and Macroscale Interactions during Substorms (THEMIS; Angelopoulos 2008) multispacecraft data from the magnetosheath. They used data from the Electrostatic Analyzer (ESA) for 7 eV–25 keV (McFadden et al. 2008) and from the Solid State Telescope (SST) for 30%–700% keV electrons (Angelopoulos 2008). In all three events, electron energy fluxes between a few hundred eV to around 10 keV were found to be increased ahead of a jet-driven bow wave. In one of the events fluxes of energies up to a few hundred keV were increased. Using THEMIS data, Liu et al. (2020a) found that around 13% of jets were driving bow waves/shocks. They reported that, statistically, the electron energy flux above ~100 eV in the ESA range is on average 2 times larger for jets with bow waves compared to the fluxes measured in the background magnetosheath preceding all observed jets. However, they did not directly compare the flux at each bow wave to the background flux of that event. Such statistical analysis is difficult to do due to instrumental resolution and challenges related to the systematic selection of jet and background windows in highly dynamic magnetosheath, etc. We believe that simulations can help us better understand this acceleration process and its constraints.

Here, we present a model of electron acceleration at jet-driven bow waves. We apply Monte Carlo test-particle simulations (e.g., Jones & Ellison 1991) of the first-order Fermi mechanism: a bow wave acts as a moving magnetic mirror, reflecting and accelerating the particles. This mechanism is amplified by a collapsing magnetic trap that the bow wave forms together with the magnetopause or some other standing magnetic mirror in the magnetosheath. We investigate how pitch-angle scattering, the bow wave speed, and magnetosheath conditions affect the efficiency of the acceleration.

2. Simulation

The simulation geometry is sketched in Figure 1(a). It includes a moving bow wave and a fixed magnetopause and follows electrons along a single magnetic field line (or in a flux

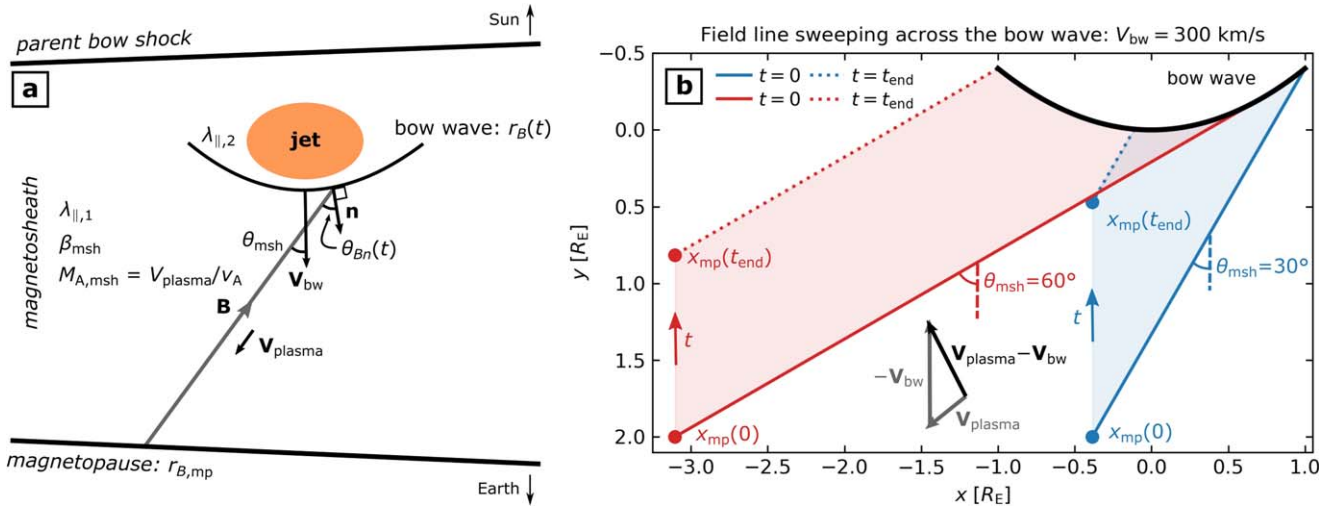

Figure 1. (a) The simulation geometry with the key parameters in the magnetopause-fixed frame. The simulation follows a magnetic field line between the jet-driven bow wave and the magnetopause in the magnetosheath, which has the following parameters: flow velocity $\mathbf{V}_{plasma}$, parallel mean free path $\lambda_{||,1}$, plasma beta β_{msh}, and Alfvén Mach number $M_{A,msh}$. As the bow wave moves with velocity $\mathbf{V}_{bw}$, the field line (inclined at θ_{msh} with respect to the jet velocity) sweeps across it, and the local shock properties (e.g., θ_{Bn} and magnetic compression ratio r_B) change. The downstream mean free path is $\lambda_{||,2}$. The magnetic compression ratio of the magnetopause is $r_{B,mp}$. (b) Field line sweeping is illustrated for $V_{bw} = 300$ km s^{-1} bow wave with $\theta_{msh} = 30°$ (blue) and 60° (red) in the bow wave rest frame. $V_{plasma} = 50$ km s^{-1} and this velocity is aligned with the field line in both cases (toward the magnetopause). The solid and dotted line segments represent the field lines at the start and end of the simulations, respectively. The dots show the intersections of the field line and the magnetopause at the start and end. The flow velocity is $\mathbf{V}_{plasma} - \mathbf{V}_{bw}$ in this frame (vectors chosen arbitrarily).

tube) between them. The field line is inclined with an angle θ_{msh} with respect to the bow wave propagation direction. We apply the guiding-center approximation, i.e., we do not follow particles' gyromotion. This approximation can be expected to hold reasonably well, as the gyroradii of electrons are small in typical magnetosheath conditions ($\lesssim$200 km for $<$1 MeV electrons $B \gtrsim 10$ nT) with respect to the system scale of this simulation. Guiding-center drifts are neglected. The particles' parallel velocities along the field line are written as $v_{||} = v\mu$, where $\mu = \cos\alpha \in [-1, 1]$ and α is the pitch angle of the particle. $\mu = 1$ is defined as the velocity vector being parallel to the magnetic field vector and $\mu = -1$ antiparallel. The guiding centers of the electrons move along the magnetic field and the electrons undergo pitch-angle scattering due to magnetic fluctuations, which are assumed to have zero phase speed in the rest frame of the magnetosheath plasma flow. This assumption may not be reasonable for all waves that scatter electrons in the magnetosheath. However, according to our tests, the simulation results are not sensitive to the wave phase speed, i.e., the speed of the fluctuations. The plasma velocity is set to be aligned with the magnetic field so that $\boldsymbol{E} = -\boldsymbol{V}_{plasma} \times \boldsymbol{B} = 0$, and the speed is set to a representative dayside magnetosheath flow value $V_{plasma} = 50$ km s^{-1}.

The scattering is assumed to be isotropic, and the upstream (denoted with index 1) parallel mean free path is set to $\lambda_{||,1} = 1,000\, R_E \approx 0.04$ au, which means that the scattering rate is very low. In comparison, the typical electron mean free path in the solar wind is $\gtrsim$0.1 au. Studies by Palmer (1981) and Bieber & Stone (1982) reported a value of the order of $\sim 1\, R_E$ for $>$200 keV electrons. However, more recent studies by Mitchell et al. (2012); Mitchell & Schwartz (2014) investigated electrons traversing the magnetosheath from one flank to another along a field line, and found no indications of strong scattering when comparing the velocity distributions at these different locations. A parameter study was performed, and lowering the mean free path below 1000 R_E (i.e., increasing the scattering rate) led to a very quick loss of high-energy particles

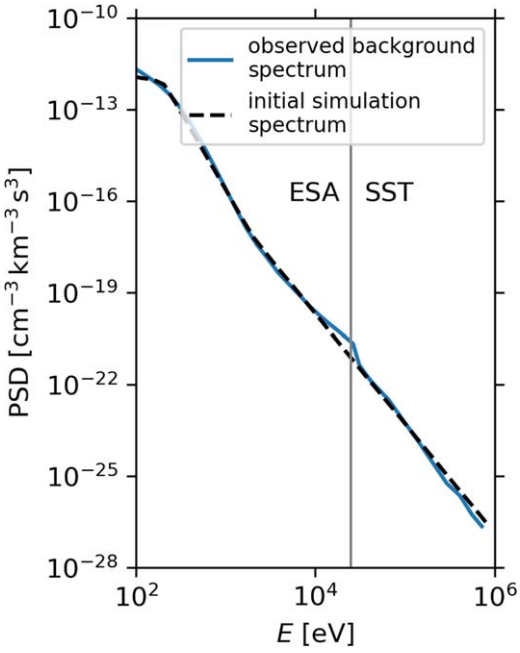

Figure 2. Background magnetosheath electron phase space density spectrum from Event 3 of Liu et al. (2020b; solid blue line) and the initial spectrum in the simulation (black dashed line). Energies left (right) of the vertical gray line have been measured by THEMIS ESA (SST) instrument.

and relatively strong acceleration of lower-energy particles, neither of which are supported by previous observations by Liu et al. (2020b, 2020a). As the mean free path is an open parameter, we show how the results change when we apply an energy-dependent mean free path in the Appendix.

At $t = 0$, the electrons are added uniformly on the field line. The initial pitch-angle cosines are also generated from a uniform distribution $\mathcal{U}(-1, 1)$ in the upstream plasma frame. In Figure 2, the dashed black curve shows the initial two-part

power-law energy distribution in the laboratory frame (the magnetopause-fixed frame) with a flat low-energy thermal part, similar to the background energy distribution of Event 3 observed by Liu et al. (2020b) in the spacecraft frame (solid blue curve). The initial energies range between 0.1 keV and 1 MeV. As we follow electrons of up to relativistic energies, we apply Lorentz transformations between the various frames of reference.

When a particle meets either the bow wave or the magnetopause, it can be magnetically mirrored or transmitted through. Particles are transmitted if their pitch angles are in the loss cone. This is determined by the ratio of the magnetic field strengths upstream and downstream of the boundary, i.e., the magnetic compression ratio r_B. The transmission condition in the de Hoffmann–Teller frame (H-T frame) of the mirror (the bow wave or the magnetopause) is

$$|\mu| > \sqrt{1 - \frac{1}{r_B}}, \tag{1}$$

given that the velocity is toward the mirror. If the particle is mirrored, its parallel velocity is reversed: $\mu \rightarrow -\mu$. If the particle is transmitted through the magnetopause, it is removed from the simulation. However, a particle transmitted to the downstream region of the bow wave can return back upstream. This return of particles is treated with a probability of return and a downstream residence time. The probability of return for a particle with speed v' (in the downstream plasma frame) is

$$P_{\rm ret} = \left(\frac{v' - u_2}{v' + u_2}\right)^2, \tag{2}$$

where u_2 is the downstream (denoted with index 2) plasma speed in the H-T frame (Jones & Ellison 1991). The downstream residence time $t_{\rm res}$ is calculated using a decay model:

$$f(t_{\rm res}) = \frac{\exp\left(-t_{\rm res}/\tau_2\right)}{\tau_2}. \tag{3}$$

Here

$$\tau_2 = \frac{4\lambda_2}{3u_{2n}} \tag{4}$$

is the mean downstream residence time, where $\lambda_2 = \lambda_{||,2}\cos^2\theta_{Bn,2}$ is the downstream mean free path along the shock normal (e.g., Drury 1983). $\theta_{Bn,2}$ is the angle between the angle between local shock normal and the downstream magnetic field and u_{2n} is the downstream flow speed along the shock normal. The downstream parallel mean free path is set at 10% of the upstream parallel mean free path: $\lambda_{||,2} = 0.1\lambda_{||,1}$. This is a model parameter fixed out of convenience, as the transmission of magnetic fluctuations into the downstream of oblique shocks is beyond the scope of this work. This parameter only becomes relevant for low mean free paths $\sim 10\,R_{\rm E}$.

The bow wave is modeled as a parabola: $y = -0.4\,R_{\rm E}^{-1}x^2$, $x \in [-1.0,\ 1.0]\,R_{\rm E}$ (see Figure 1(b)). The simulation starts when the field line first touches the bow wave, and the magnetopause end of the field line is set to be at the $y = 2\,R_{\rm E}$ vertical distance from the nose of the bow wave. This distance is comparable to the width of the magnetosheath. As the bow wave moves through an oblique background magnetic field, the local shock parameters change. The shock obliquity angle $\theta_{Bn,1}$ between the local shock normal and the upstream magnetic field (denoted just as θ_{Bn} from here onwards) can be computed analytically. The local magnetic compression ratio r_B of the bow wave is calculated using MHD solutions for oblique shocks (e.g., Priest 1982). The density compression ratio r is first solved from the cubic equation by using a polynomial fit. In the future, we aim to incorporate a more realistic shock structure into our model. At that time, considering the gyromotion of electrons may become important. The simulation stops when the field line meets the edge of the bow wave (see Figure 1(b) red dotted line) or when the magnetopause end of the field line is at $y = 3000$ km (blue dotted line).

The magnetopause is approximated to be a flat plane (or a straight line) in the spatial scales of interest here. Its magnetic compression ratio is set to $r_{B,\rm mp} = 10$. This makes the magnetopause a very efficient reflector, but makes up for the lack of particle sources in the simulation. In reality, magnetospheric particles can leak into the magnetosheath through the magnetopause and magnetopause reconnection at the dayside magnetopause may affect this leakage. The role of these sources was unclear in the events studied by Liu et al. (2020b).

We present results of multiple simulation runs varying the bow wave speed $V_{\rm bw}$ (given in the magnetopause-fixed frame) and magnetosheath parameters $\theta_{\rm msh}$, $\beta_{\rm msh}$, and directionless Alfvén Mach number:

$$M_{\rm A,msh} = \frac{V_{\rm plasma}}{v_{\rm A}} = V_{\rm plasma}\frac{\sqrt{\mu_0\rho_1}}{B_1}. \tag{5}$$

Here, $v_{\rm A}$ is the Alfvén speed in the magnetosheath. The bow wave speed gets values 200, 300, and 400 km s^{-1}; a range that represents bow waves as observed by Liu et al. (2020a). The magnetosheath field obliquity $\theta_{\rm msh}$ gets values 30° and 60°. The latter corresponds to a typical field obliquity ahead of a jet according to Plaschke et al. (2020b). We use two plasma beta and directionless Alfvén Mach number combinations ($\beta_{\rm msh}$, $M_{\rm A,msh}$), (8, 1) and (3, 0.5), which have been selected as representative values of THEMIS spacecraft observational data from the subsolar magnetosheath. The fast magnetosonic Mach numbers of the simulated bow waves vary between 1 and 3 (not shown).

3. Results

Figure 3 shows the time evolution of θ_{Bn} and r_B at the bow wave in different simulation runs. To investigate how much the electron energy flux has increased during the simulation, we show the ratios of peak fluxes and the background fluxes at $t = 0$ (i.e., peak fluxes normalized by initial fluxes). The peak spectrum is determined by finding the time when the mean of energy flux ratios of all energies is at its maximum. These fluxes have been averaged over the whole flux tube. Overall, for simulations with $\theta_{\rm msh} = 30°$, the peak fluxes occur after $\sim$20 s, while for $\theta_{\rm msh} = 60°$ they occur at the very beginning of the simulations. Figures 3(a) and (d) show that when the bow wave is faster, the field line sweeps across it in less time. Thus, θ_{Bn} changes more rapidly for faster bow waves. Figures 3(b) and (e) show that the fastest bow waves with more favorable magnetosheath plasma conditions ($\beta_{\rm msh} = 8$ and $M_{\rm A,msh} = 1$) reach the largest r_B. Higher r_B leads to higher energy flux ratios —stronger acceleration. We can see that the peak spectra in both Figures 3(c) and (f) are clearly ordered by bow wave

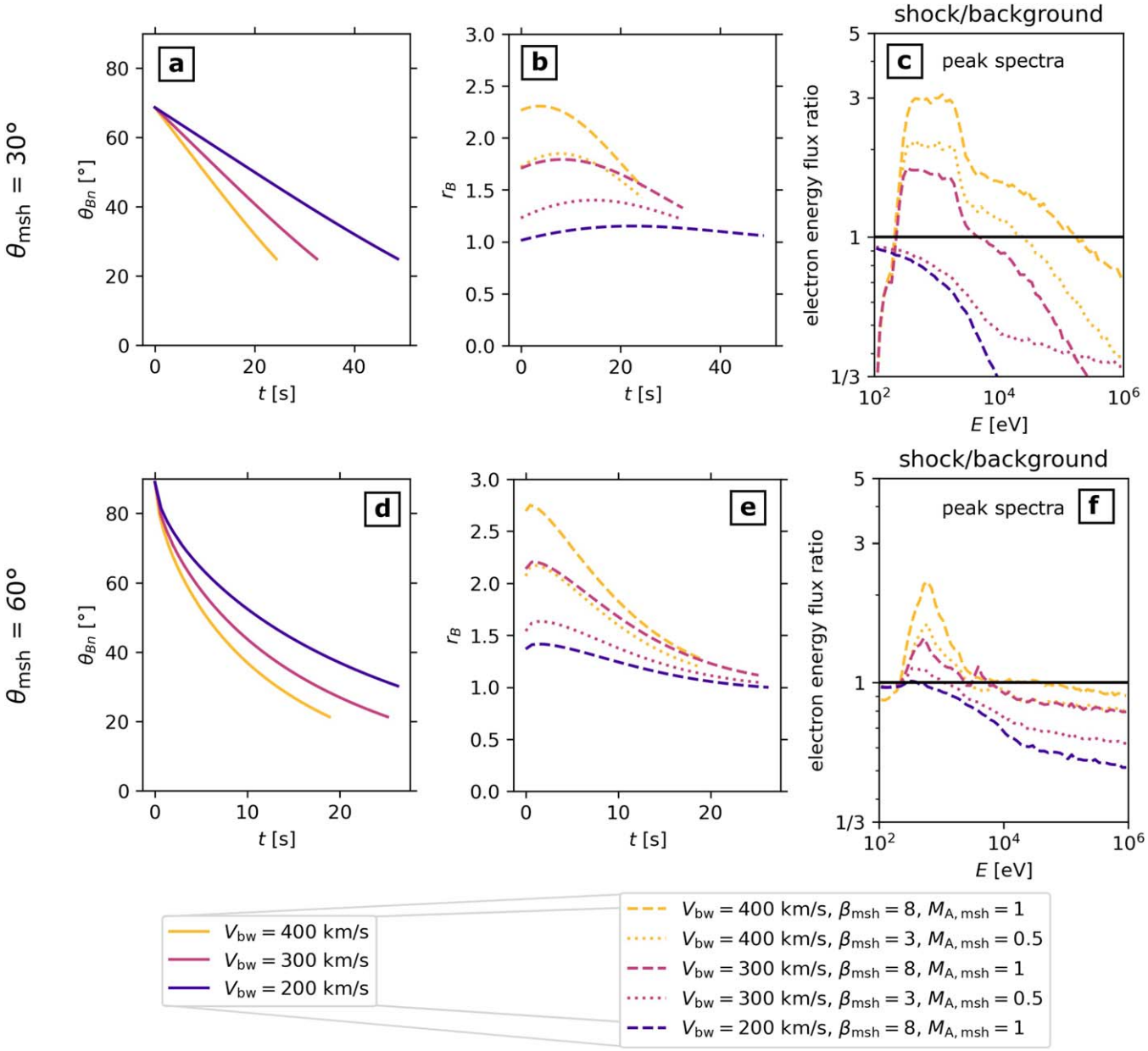

Figure 3. Simulation runs with (a)–(c) $\theta_{msh} = 30°$ and (d)–(f) 60°. (a) and (d) The local θ_{Bn} as a function of time for the three different bow wave speeds: 400, 300, and 200 km s^{-1}. (b) and (e) The magnetic compression ratio of the bow wave as a function of time for bow waves of different speeds with ($\beta_{msh} = 8$, $M_{A,msh} = 1$; dashed line) and ($\beta_{msh} = 3$, $M_{A,msh} = 0.5$; dotted line). (c) and (f) The peak energy spectra of each simulation run divided by the initial spectrum of the simulation.

speed and for the same bow wave speed and, thus, for the same θ_{Bn} time profile, acceleration is more efficient when $\beta_{msh} = 8$ and $M_{A,msh} = 1$ than when $\beta_{msh} = 3$ and $M_{A,msh} = 0.5$. The bow waves typically accelerate electrons that have energies of a few hundred eV to 10 keV. The factor by which the fluxes of these electrons increase is 2–3 for $\theta_{msh} = 30°$ and 1–2 for $\theta_{msh} = 60°$. Electrons with energies larger than 10 keV are efficiently lost from the flux tube. However, the combination of parameters $\theta_{msh} = 30°$, $V_{bw} = 400$ km s^{-1}, $\beta_{msh} = 8$, and $M_{A,msh} = 1$ results in acceleration of electrons with energies up to 100 keV (dashed yellow line in Figure 3(c)).

In Figure 4, we show the time evolution of pitch-angle cosine distributions in different energy channels. The upper panels represent a run with $\theta_{msh} = 30°$ and the lower panels a run with $\theta_{msh} = 60°$. The other simulation parameters are equal for both runs: $V_{bw} = 300$ km s^{-1}, $\beta_{msh} = 8$, and $M_{A,msh} = 1$. In each panel, the units are electron energy fluxes normalized to the energy fluxes of the energy channel at $t = 0$. Comparing the electrons of different energy channels, we can see they behave very differently. Particles with $|\mu|$ close to 1 are in the loss cone (see the white regions with ratios <0.25). The magnetopause reflects efficiently but the particles are usually lost at the bow wave. Higher-energy electrons (panels (c) and (d), and (g) and (h)) move faster between these two boundaries so they enter the loss cone quicker than low-energy particles (panels (a) and (b), and (e) and (f)). The bow wave pushes particles out of the region with $\mu \sim 0$ by increasing their parallel speed, and this is more efficient for low-energy particles, because the velocity change is relatively larger. Particles also experience pitch-angle scattering which can take them into the loss cone.

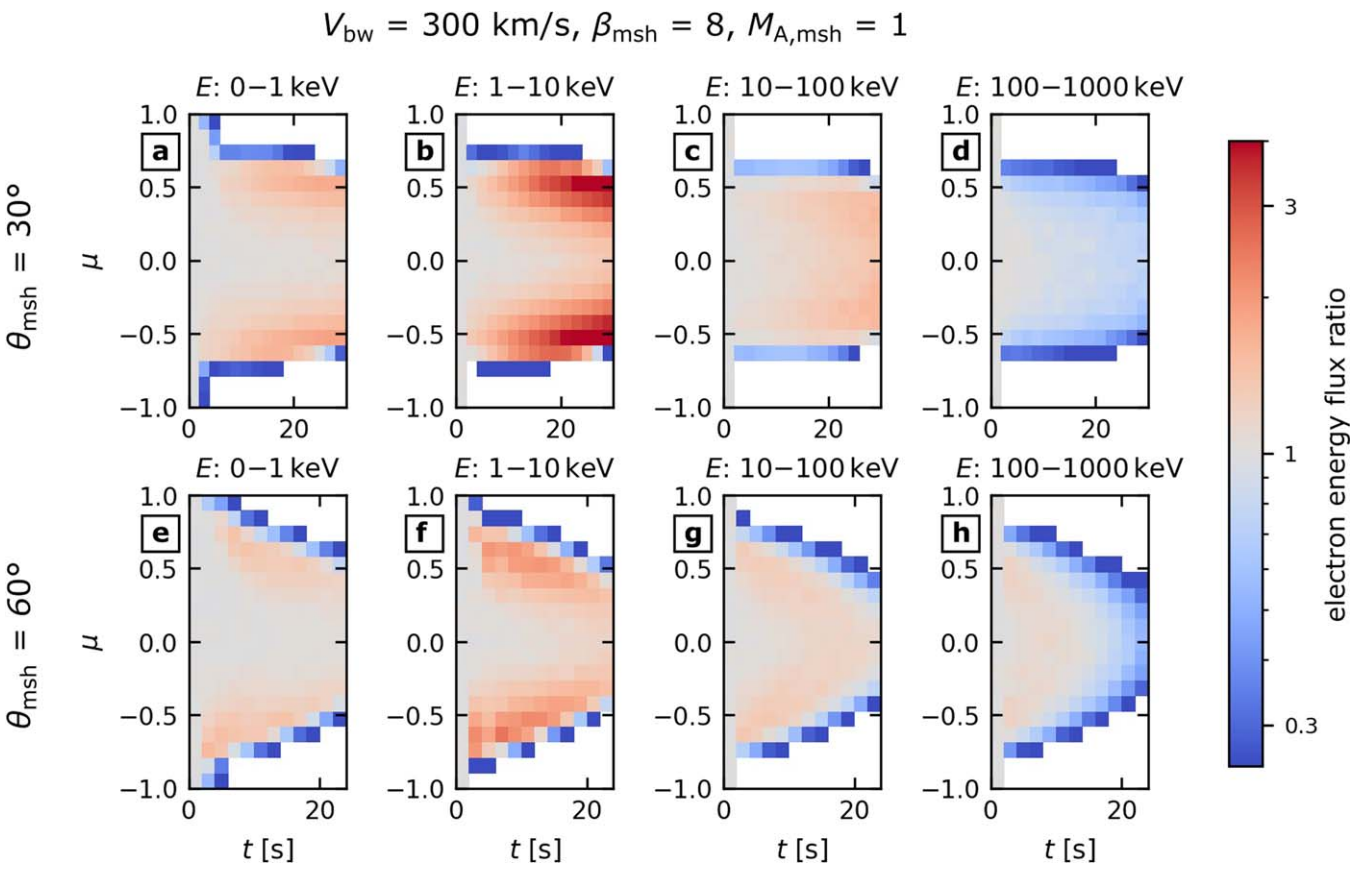

Figure 4. 2D maps of the simulation runs with $V_{bw} = 300$ km s^{-1}, $\beta_{msh} = 8$, $M_{A,msh} = 1$, for (a–d) $\theta_{msh} = 30°$ and (e–h) $\theta_{msh} = 60°$. The maps show the time evolution of pitch-angle cosine $\mu = \cos\alpha$ distribution of electrons in different energy channels. The units are intensities normalized to the intensity at $t = 0$ in each energy channel. $\mu > 0$ is toward the bow wave and $\mu < 0$ is toward the magnetopause. White cells have energy flux ratios below the colorbar scale: <0.25.

Panels (a)–(b) and (e)–(f) show the presence of both antisunward and sunward beams. We can see that for the run with $\theta_{msh} = 60°$, the fluxes peak much earlier than for the run with $\theta_{msh} = 30°$. Particles that can stay in the flux tube for an extended period of time are accelerated by the bow wave and their intensity can increase as the magnetic trap keeps collapsing. From the beginning of the simulation run until the end, the length of the flux tube is contracted by a factor of ∼5 (∼2) for $\theta_{msh} = 30°$ (60°). For $\theta_{msh} = 30°$, the flux increases are more gradual and indicate that the collapse of the trap is an important factor. In contrast, for $\theta_{msh} = 60°$, the fluxes peak at the beginning when the local θ_{Bn} is very high and particles are efficiently accelerated during an interaction with the bow wave. A single interaction leads to a larger relative energy increase of the particle for lower-energy particles than for higher-energy particles.

4. Discussion and Conclusions

We have developed a Monte Carlo test-particle model of electron acceleration on a field line between a jet-driven bow shock and the magnetopause. The model includes the following physics elements: a collapsing magnetic trap with a shock at one end and pitch-angle scattering inside the region between the shock and the magnetopause as well as downstream of the bow wave. We investigated the relative importance of these elements, comparing the resulting spectra to observations. We found that the collapsing magnetic trap is a crucial element to keep particles accelerating for long enough, with particles interacting with the shock many times. We found that at these spatial/temporal scales scattering plays a minor role and best match between the model and the observations is with weak scattering. While stronger scattering may enhance acceleration by allowing particles to return from downstream to upstream, we confirmed the weak role of scattering by also running test simulations without scattering. Fluxes of higher-energy particles are in fact more enhanced when scattering is turned off, as they can stay longer in the magnetic trap. Therefore, the acceleration is due to the collapsing trap between the bow wave and the magnetopause with shock drift acceleration (SDA) at the moving bow wave. In SDA, particles gain energy from the convective electric field as they drift along the shock due to magnetic gradients at the shock. SDA is important when the local θ_{Bn} is high (thus, especially for the case with $\theta_{msh} = 60°$, for which the fluxes peak quickly in the simulations). All in all, the source of free energy is the relative motion of the jet through the magnetosheath. We find that these bow waves are typically able to accelerate electrons from a few hundred eV to around 10 keV. At best, bow waves can increase the energy flux of up to a few hundred keV electrons. The factor by which bow waves can increase the energy flux is between 1 and 3.

The speed of the bow wave is a significant parameter for the efficiency of the acceleration, but magnetosheath conditions also contribute greatly. The geometry of the event affects the acceleration. When the background magnetic field is highly oblique, the interaction time between the bow wave and the field line is short, and the acceleration is limited even though the shock drift acceleration mechanism is the strongest for high

θ_{Bn}. Due to these short timescales, observations would greatly benefit of subsecond instrumental resolutions.

The initial length of the flux tube also affects the observed acceleration. When the bow wave meets a field line closer to the magnetopause, the number of times the electrons can interact with the high θ_{Bn} part of the bow wave is higher before being lost. In addition to the simulations shown here with the magnetopause end of the field line initially at $y = 2\,R_E$, we have simulated such field lines closer to the magnetopause, and the flux increases are indeed higher (not shown). For example, with an initial distance of $y = 1\,R_E$ even the fluxes of 0.1–1 MeV electrons can be increased by a factor of ∼1.5–2 with the combination $V_{bw} = 400$ km s^{-1}, $\beta_{msh} = 8$, and $M_{A,msh} = 1$, both for $\theta_{msh} = 30°$ and $\theta_{msh} = 60°$. Overall, the highest flux increases have been around a factor of 5 for ∼1 keV electrons.

The model presented here is simple in comparison to the observed complicated structure of these bow waves (Liu et al. 2019, 2020b). The bow waves are MHD shocks and kinetic processes that may be important are not included. For instance, MHD shocks do not exhibit overshoots, which are often observed in turbulent shocks, and we do not include the cross-shock potential in our model. Furthermore, plasma instabilities can amplify the magnetic field and scattering conditions near the shock (e.g., Bell 2004; Riquelme & Spitkovsky 2009; Caprioli & Spitkovsky 2014a, 2014b, 2014c; Park et al. 2015; Gupta et al. 2021), particularly at high-M_A shocks. However, for the low-Mach bow waves and the short timescales considered here, the significance of these instabilities can be expected to be small. All these kinetic elements influence particle movement at the shock, and thus the shock's ability to reflect particles and accelerate them via the shock drift acceleration mechanism.The structure does not have to be a shock either to facilitate particle acceleration. A bow wave that is not yet not fully developed to a shock may still exhibit a magnetic compression large enough to keep particles trapped for a sufficient amount of time to be accelerated via the Fermi mechanism. Thus, when using MHD solutions, the magnetic compression ratios may be underestimated for a given bow wave speed. Overall, the magnetic compression ratios 1–3 seen here correspond well with those in the events studied by Liu et al. (2019, 2020b). Despite its limitations, our model can provide qualitative understanding of the electron acceleration at jet-driven bow waves and quantitative results that may represent this process statistically.

The magnetopause magnetic compression ratio is set to 10. Changing the parameter to a more realistic value of 2 produces very similar results. Only the high-energy tails become steeper as particles are lost from the flux tube more quickly. We have also fixed the bow wave size here to one that would form in front of a typical large-scale jet (Plaschke et al. 2016, 2020a). Jets can be even larger, and the larger the bow wave, the longer the interaction time of the field line with the quasi-perpendicular shock region, and the more efficient the acceleration. Many jets are smaller and their contribution to electron acceleration would be smaller.

Electron mean free path is still not well known in the magnetosheath. We have presented results using $\lambda_{||,1} = 1,000\,R_E$. The mean free path $\lambda_{||,2}$ downstream of the bow wave is set to 10% of $\lambda_{||,1}$ (thus, to $100\,R_E$). Decreasing the downstream mean free path may increase acceleration as particles can more easily return back upstream after being transmitted downstream. However, decreasing it to 1% has a negligible effect when the upstream scattering rate is low ($\lambda_{||,1} \gtrsim 100\,R_E$). If we instead decrease $\lambda_{||,1}$, the qualitative results remain: for higher obliquity $\theta_{msh} = 60°$, particles are accelerated efficiently during the first seconds of the simulation, but for $\theta_{msh} = 30°$ the fluxes peak after around 20 s in the simulation. Energy flux ratios below 10 keV reach higher values but higher-energy electrons are quickly lost. To observe flux increases for electrons of >10 keV in our simulations, $\lambda_{||,1}$ has to be high. This is because stronger scattering boosts loss from the flux tube. Additionally, while Fermi process increases the parallel speed of the particle, scattering converts some of that into perpendicular speed and keeps the bounce rate between the two mirrors lower, consequently decreasing acceleration (Liu et al. 2017). All in all, electron acceleration is observed for all reasonable values of 1–1000 R_E. Results for simulations with energy-dependent mean free paths can be found in the Appendix.

Previous observational studies have demonstrated that bow waves driven by fast magnetosheath jets can lead to further acceleration downstream of the Earth's bow shock. Our simulations suggest that the energy increase of suprathermal electrons can be explained by by a collapsing trap forming between the moving bow wave and the magnetopause or another standing mirror in the magnetosheath, with shock drift acceleration at the bow wave. Pitch-angle scattering is found to be unimportant. In the future, we aim to further improve our model by adding a more realistic magnetic field structure ahead of the bow wave, and by working toward including the downstream region of the bow wave into our simulation. In addition, future observational studies are needed to provide better constraints for the parameters, especially related to scattering both upstream and downstream of the bow wave and to particle sources at the magnetopause. Modern multispacecraft missions such as the Magnetospheric Multiscale Mission (MMS) can help us study these problems in the required spatial and temporal detail.

The work in the University of Turku was performed in the framework of the Finnish Centre of Excellence in Research of Sustainable Space (FORESAIL) funded by the Academy of Finland (grants 309939 and 336809). L.V. acknowledges the support of the University of Turku Graduate School and the Finnish Academy of Science and Letters (Väisälä Fund). H.H. was supported by the Royal Society award URF\R1\180671.

Appendix
Energy-dependent Mean Free Path

In Figure 5, we show the peak spectra of simulations with energy-dependent mean free paths similar to Figures 3(c) and (f). The energy dependence is assumed to be a power law in momentum:

$$\lambda_{||,1} = \lambda_0 (p/p_0)^a, \tag{A1}$$

where $\lambda_{||,1}$ is again the parallel upstream mean free path of an electron with momentum p (energy E), a is the power-law index, and λ_0 is the parallel upstream mean free path of an electron with momentum p_0 (energy E_0). Figure 5(a) shows the upstream mean free path as a function of electron energy for five different power laws, where the mean free paths are within the range of magnitudes 10–1000 R_E. Figures 5(b)–(f) (Figures 5(g)–(k)) show the corresponding peak spectra for

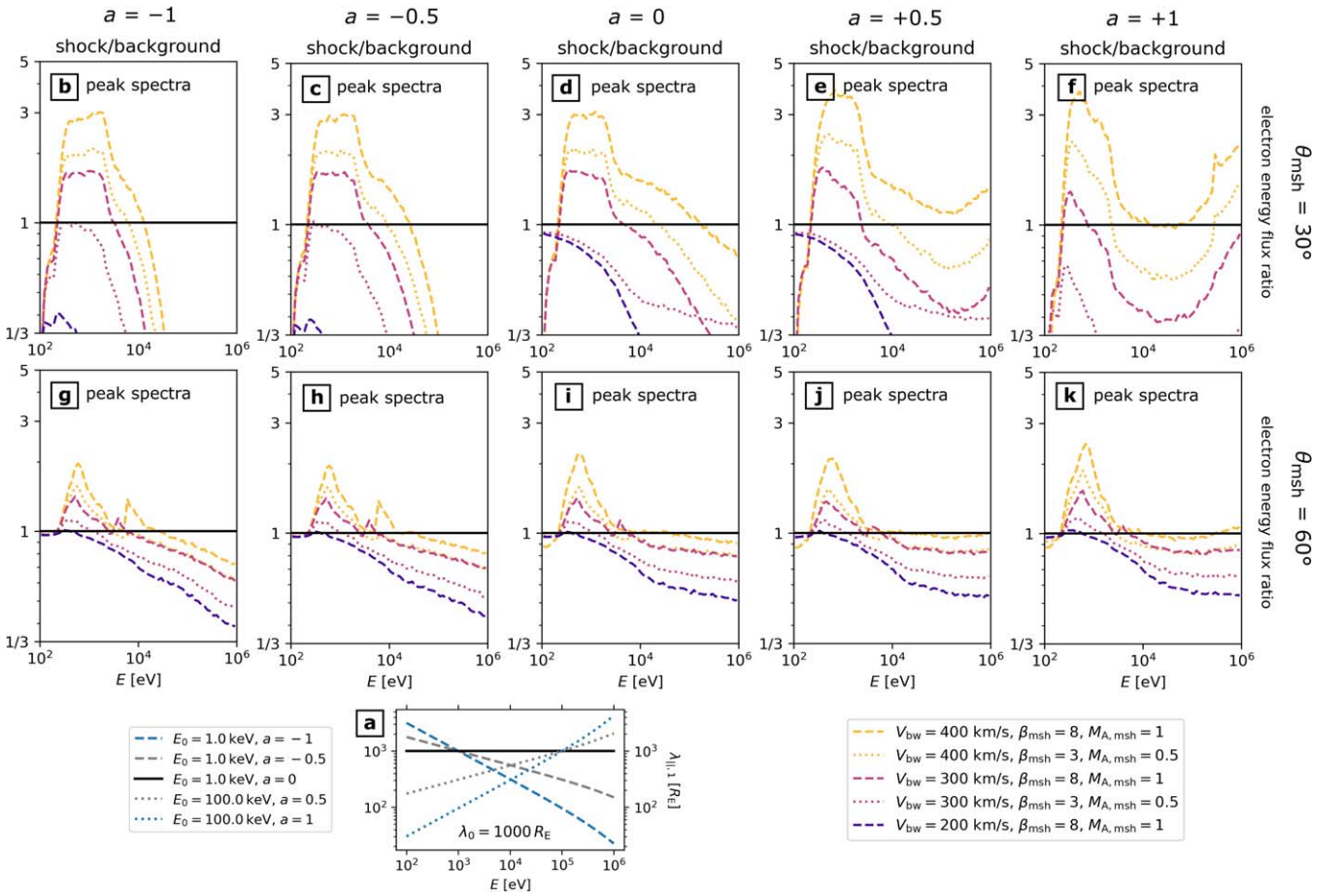

Figure 5. (a) Five different power laws for the electron parallel upstream mean free path $\lambda_{||,1}$ as a function of energy (Equation (A1)). (b)–(f) Peak spectra for simulations with $\theta_{msh} = 30°$, using these different power laws for the mean free path (each column corresponds to a different power law, identified by the spectral index a). (g)–(k) Peak spectra for the simulations with $\theta_{msh} = 60°$.

simulations with $\theta_{msh} = 30°$ ($\theta_{msh} = 60°$). We can see that while the fluxes of <10 keV electrons are enhanced regardless of the value of mean free path, the fluxes of high-energy electrons are only enhanced when the mean free path is high. In particular, the quick interaction of electrons with the highly oblique bow wave in simulations with $\theta_{msh} = 60°$ is not affected by the mean free path.

ORCID iDs

Laura Vuorinen https://orcid.org/0000-0002-2238-109X
Rami Vainio https://orcid.org/0000-0002-3298-2067
Heli Hietala https://orcid.org/0000-0002-3039-1255
Terry Z. Liu https://orcid.org/0000-0003-1778-4289

References

Angelopoulos, V. 2008, SSRv, 141, 5
Archer, M. O., & Horbury, T. S. 2013, AnGeo, 31, 319
Bell, A. R. 2004, MNRAS, 353, 550
Bieber, J. W., & Stone, E. C. 1982, JGRA, 87, 85
Caprioli, D., & Spitkovsky, A. 2014a, ApJ, 783, 91
Caprioli, D., & Spitkovsky, A. 2014b, ApJ, 794, 46
Caprioli, D., & Spitkovsky, A. 2014c, ApJ, 794, 47
Drury, L. O. 1983, RPPh, 46, 973
Gupta, S., Caprioli, D., & Haggerty, C. C. 2021, ApJ, 923, 208
Hietala, H., Laitinen, T. V., Andréeová, K., et al. 2009, PhRvL, 103, 245001
Jones, F. C., & Ellison, D. C. 1991, SSRv, 58, 259
LaMoury, A. T., Hietala, H., Plaschke, F., Vuorinen, L., & Eastwood, J. P. 2021, JGRA, 126, e29592
Liu, T. Z., Hietala, H., Angelopoulos, V., et al. 2019, GeoRL, 46, 7929
Liu, T. Z., Hietala, H., Angelopoulos, V., et al. 2020a, JGRA, 125, e27710
Liu, T. Z., Hietala, H., Angelopoulos, V., Vainio, R., & Omelchenko, Y. 2020b, JGRA, 125, e27709
Liu, T. Z., Lu, S., Angelopoulos, V., Hietala, H., & Wilson, L. B., III 2017, JGRA, 122, 9248
McFadden, J. P., Carlson, C. W., Larson, D., et al. 2008, SSRv, 141, 277
Mitchell, J. J., & Schwartz, S. J. 2014, JGRA, 119, 1080
Mitchell, J. J., Schwartz, S. J., & Auster, U. 2012, AnGeo, 30, 503
Palmer, I. D. 1981, JGR, 86, 4461
Park, J., Caprioli, D., & Spitkovsky, A. 2015, PhRvL, 114, 085003
Plaschke, F., Hietala, H., & Angelopoulos, V. 2013, AnGeo, 31, 1877
Plaschke, F., Hietala, H., Angelopoulos, V., & Nakamura, R. 2016, JGRA, 121, 3240
Plaschke, F., Hietala, H., & Vörös, Z. 2020a, JGRA, 125, e27962
Plaschke, F., Jernej, M., Hietala, H., & Vuorinen, L. 2020b, AnGeo, 38, 287
Plaschke, F., Hietala, H., Archer, M., et al. 2018, SSRv, 214, 81
Priest, E. R. 1982, Shock Waves (Dordrecht: Springer), 189
Riquelme, M. A., & Spitkovsky, A. 2009, ApJ, 694, 626
Vuorinen, L., Hietala, H., & Plaschke, F. 2019, AnGeo, 37, 689